

# Optimal operating parameters for next-generation xenon gas time projection chambers

---

**K. Mistry,<sup>1</sup> D.R. Nygren,<sup>1</sup>**

<sup>1</sup>*Department of Physics, University of Texas at Arlington, Arlington, TX 76019, USA*

*E-mail:* [krishan.mistry@uta.edu](mailto:krishan.mistry@uta.edu)

**ABSTRACT:** The next-generation of neutrinoless double beta decay ( $0\nu\beta\beta$ ) searches are targeting half-life sensitivities towards  $10^{27}$ – $10^{28}$  years. Gaseous xenon time projection chamber (GXeTPC) detectors are a technology that may be able to meet this challenge due to their excellent background rejection power, scalability, and energy resolution. This paper explores how the design choices of a next-generation GXeTPC time projection chamber can impact the overall performance of the experiment. We study the performance of systems using xenon enriched in the isotope  $^{136}\text{Xe}$  or natural xenon, focusing on scenarios that incorporate one tonne of source isotope. The detector size, copper shielding mass, energy resolution, pressure, and diffusion amount are surveyed to evaluate the overall performance dependencies on these parameters. A detector optimized for using enriched xenon is preferred, with a factor of 10 lower background rate, driven by the large intrinsic backgrounds introduced by the copper shielding used in the detector. The performance of three types of gas TPC technologies was also explored based on different gas additives used to reduce diffusion to different levels. For all TPC technologies, we find background rates of a fraction of a count per tonne year in the region of interest are achievable. These performances are contingent on suitable energy resolution and event position placement in the drift direction being achieved for the specific detector technology. When factoring in the considerations for the construction of the detector in addition to the selection performance, there is no clear optimum pressure, with advantages and disadvantages if a high or low pressure default configuration is chosen.

---

## Contents

<b>1</b>	<b>Introduction</b>	<b>1</b>
<b>2</b>	<b>Detector Design Considerations</b>	<b>2</b>
2.1	Detector Design Challenges	3
2.2	Detector Technology	4
2.3	Analysis Challenges	6
<b>3</b>	<b>Detector Simulation and Geometry</b>	<b>7</b>
<b>4</b>	<b>Analysis</b>	<b>10</b>
4.1	Containment Efficiencies	10
4.2	Energy Resolution	13
4.3	Reconstruction	13
4.4	Selection Diffusion Dependence	15
4.5	Selection Pressure Dependence	15
<b>5</b>	<b>Results</b>	<b>17</b>
5.1	Acceptance and Rate with Diffusion and Pressure	17
5.2	EL TPC	18
5.3	Topology TPC	18
5.4	Ion TPC	19
<b>6</b>	<b>Discussion and Summary</b>	<b>20</b>
<b>A</b>	<b>Natural Xenon Detector</b>	<b>24</b>
<b>B</b>	<b>Impact of Event Placement</b>	<b>25</b>

---

## 1 Introduction

Neutrinoless double beta decay ( $0\nu\beta\beta$ ) decay is a hypothetical rare process whereby two neutrons in a nucleus beta decay emitting two electrons, two protons and no antineutrinos. This radioactive decay is only possible if the neutrino is its own antiparticle (a Majorana fermion), in which case two virtual neutrinos can annihilate within the nucleus, giving practically all the decay energy to two outgoing beta electrons. The experimental signature is a peak at the summed beta energy end-point ( $Q_{\beta\beta}$ ) of the Standard Model two-neutrino double beta decay ( $2\nu\beta\beta$ ) spectrum. The discovery of the Majorana nature of the neutrino would help provide answers to some of the largest outstanding questions about the Universe, including why it is matter-dominated and why the neutrino mass is so light.

The best limits for  $0\nu\beta\beta$  decay to date have been obtained by the KamLAND-Zen experiment using  $^{136}\text{Xe}$  [1] reaching  $3.8 \times 10^{26}$  yr half-life at 90% confidence level (CL) and LEGEND-200 with  $^{76}\text{Ge}$  [2] reaching  $1.9 \times 10^{26}$  at 90% CL. The next generation of  $0\nu\beta\beta$  decay experiments aim to improve on these limits by a factor 10–100, targeting sensitivities towards  $10^{27}$ – $10^{28}$  years, a feat which requires one to several tonnes of source isotope.

Here, we consider the performance of a gaseous xenon time projection chamber (GX-eTPC) in the search for  $0\nu\beta\beta$  decay using  $^{136}\text{Xe}$  as the source isotope with a  $Q_{\beta\beta}$  of 2.458 MeV. The leading experiment with this technology is the NEXT experiment, which employs a high-pressure GXeTPC with electroluminescent amplification. The latest iteration in this program, NEXT-100 [3], consists of 70.5 kg of  $^{136}\text{Xe}$  at 13.5 bar pressure, and is currently operating at the Laboratorio Subterráneo de Canfranc (LSC) with expected sensitivity of the order  $10^{25}$  yr at 90% CL. NEXT-100 incorporates 1 m diameter cathode and anode planes [4], a high voltage system suitable for reaching 65 kV [5], and a gas pressure system that can handle pressures up to 15 bar [3].

The usual operation of a GXeTPC consists of a chamber filled with gaseous xenon. Charged particles, such as the beta electrons produced from  $0\nu\beta\beta$ , scatter on the gas where they ionize and excite it as they deposit energy. The excitations produce a prompt flash of scintillation light (S1), with a wavelength of  $\sim 170$  nm, that is used to determine the time of interaction. An electric field ( $E$ ) is generated in the TPC by applying a high voltage (HV) between a cathode and anode plane. This electric field drifts the ionization electrons towards the anode plane with a blurring of their original position due to diffusion. After reaching the anode plane, the ionization electron signal is amplified producing a secondary, larger signal (S2), such as using an electroluminescent (EL) amplification process. The S2 signal is used for precise energy measurement and imaging of the diffused particle track in 2D. The combination of the timing information and 2D imaging allows for a full 3D reconstruction of charged particle interactions depositing energy in the detector.

The goal of this work is to explore a variety of design and operation choices of a GX-eTPC detector. We consider a detector with a fixed isotopic source mass of one tonne and a cylindrical geometry with length equal to diameter of size  $L$ . Key variables to be surveyed include detector size, ranging from 2–13 m to account for different gas enrichment fractions, pressures from 1–25 bar, energy resolutions from 0.3%–1.2%, and diffusion-reducing gas mixtures with the addition of molecular additives or helium.

The paper is structured as follows: Sec. 2 describes the design considerations for optimizing a tonne-scale GXeTPC, Sec. 3 details the detector simulation and geometry, Sec. 4 describes the analysis. The results are shown in Sec. 5, followed by a discussion and concluding remarks in Sec. 6.

## 2 Detector Design Considerations

In the design of the GXeTPC experiment, the major considerations should take into account (i) design challenges: the feasibility of building the detector, (ii) choice of detector technology through the introduction of gas additives which can alter significantly how the TPC operates, and (iii) analysis challenges: the reduction of the overall intrinsic back-

ground to negligible levels while maintaining sufficient signal efficiency. Considering these challenges, one of the most important variables is the choice of gas pressure, with various advantages and disadvantages.

## 2.1 Detector Design Challenges

In the detector design, there are several factors that must be balanced, accounting for the engineering of the detector and overall physics capability. In this section, we describe these major factors.

**High-Pressure Gas Containment:** The vessel size scales non-linearly in cost and difficulty. Going from a meter-scale detector, with  $\sim 100$  kg mass to a tonne-scale detector of several meter size with  $\sim 1000$  kg mass increases the linear detector radius by a factor  $\sqrt[3]{10} \simeq 2.2$ . At high pressure, the force exerted on the end-caps that supports the detector scales with the square of the radius. Overall, lower pressure is favored from this mechanical engineering standpoint. Operation at 1 bar represents a unique use case, as there will be no internal force exerted by the gas.

**Detector Size:** Considering a cylindrical geometry fixed mass of source isotope, the cylinder length is given by  $L = \sqrt[3]{4M/\pi\rho P}$ , where  $M$  is the total mass of  $^{136}\text{Xe}$ ,  $\rho$  is the density of xenon at normal temperature and pressure ( $\rho = 5.987 \text{ kg/m}^3$ ), and  $P$  is the gas pressure. The detector length scales as  $1/\sqrt[3]{P}$  which favors higher gas pressures resulting with smaller detector sizes.

**Site Location:** For the  $0\nu\beta\beta$  decay search, the experiment must be built deep underground to reduce the cosmogenic backgrounds. There are several candidate locations which could site the detector, for example: SNOLAB, Boulby, LNGS, SURF, and LSC [6]. The feasibility to construct the detector must account for the available facilities at these site locations. For example, SNOLAB and SURF are deep underground and can only be accessed through a mine shaft of fixed size. This sets a maximum size that any given part, such as the end-caps, can be transported underground. One bar is advantageous for these deep site locations as parts can be more simply welded underground; however, higher-pressure is favored when considering the limited underground hall size.

**Radioactive Burden:** It is common to use a shield of low-background ( $\sim 1 \text{ }\mu\text{Bq/kg}$ ) [7] copper for the inner layer of the detector to reduce the rate of  $\sim 2.5$  MeV gamma rays entering the active volume which can deposit energy close to the  $Q_{\beta\beta}$  value. About 10-12 cm copper is sufficient to attenuate 97-99% of these backgrounds originating from outside the detector, such as the stainless steel pressure vessel. While this copper has low activity compared to materials such as stainless steel, the large mass results in it being the largest source of background for the experiment. Assuming a fixed copper thickness, the mass scales with  $L^2 \sim P^{-2/3}$ , favoring higher-pressure.

Cosmogenic muons can interact with the detector surroundings, leading to a source of neutrons that can capture and activate materials. Neutron shielding can be provided through the use of water shields, which are likely easier to construct for smaller-sized detectors.

**High Voltage:** For the detector with the same cylindrical geometry and isotopic mass, the pressure varies as  $1/L^3$ , while the maximum drift length scales as  $L$ . For generation of

the same drift field of  $E/P = 60$  V/cm/bar, the HV for 1 bar with 6 m drift is 36 kV but would be 150 kV at 10 bars and 2.5 m drift, favoring lower-pressure operation.

**Readout Plane:** The number of readout sensors increases with the square of the detector radius, favoring higher pressure. The readout plane needs to have a suitable light-collection efficiency to obtain the low energy resolution required of  $\sim 1\%$  full width at half maximum (FWHM).

**Track Clarity:** The track length scales as  $1/P$ , while the diffusion scales as  $1/\sqrt{P}$ . As the ratio of diffusion to track length is thus proportional to  $\sqrt{P}$ , this ratio favors lower pressure and improves the ability to separate signal from background due to the improved track clarity.

**Isotope Safety:** Risk of catastrophic loss of xenon due to rupture of the vessel does not exist at 1 bar pressure. Higher pressures require more complicated xenon recovery systems.

**Detector Calibration:** MeV-scale gamma rays from high-energy radioactive sources such as  $^{208}\text{Tl}$  are likely to penetrate deeper into the active volume at lower pressure, while overall statistics will be reduced due to the lower cross section with density. Calibration with low-energy sources such as  $^{83\text{m}}\text{Kr}$  will likely be harder to reconstruct at lower pressures due to the larger area of the detector and lower S1 reconstruction efficiency.

**Additional Physics Probes:** In the event of positive observation of  $0\nu\beta\beta$  decay, this would prove the neutrino is a Majorana particle; however, the underlying physics that drives the decay would still be unknown. Such physics could be probed in GXeTPCs [8] by identifying the decay vertex and extracting kinematic information such as the individual beta electron energies and angle. Extracting this information favors low-pressure where there is a higher track clarity.

## 2.2 Detector Technology

The use of gas additives can significantly change the operation of the detector, impacting a variety of different properties with advantages and disadvantages. We consider three modes of operation, considering gas additives that alter the diffusion extent but also the fundamental detector gas technology where certain technologies are more well-established than others. These include (i) noble element gas additives for an *Electroluminescent TPC*, (ii) molecular gas additives for a *Topology TPC*, and (iii) near diffusion-free tracks for an *Ion TPC*.

**Electroluminescent TPC:** An electroluminescent TPC preserves the use of VUV scintillation light and the use of the S1/S2 signals through the use of pure xenon or xenon-noble-element gas mixtures. This includes the well-established NEXT TPC technology [7]. Such detectors have demonstrated energy resolutions below 1% FWHM and plausibly could reach resolutions towards 0.5% FWHM [9, 10]. Furthermore, the timing difference between the S1 and S2 signals is an effective method for obtaining 3D reconstruction of event positions that can be used for rejecting radon induced backgrounds to negligible levels (see Sec. 2.3).

The use of  $^4\text{He}$  can be used for reducing the transverse diffusion by about a factor of two compared with pure xenon while also being compatible with EL with reductions in the

total yield by up to 2-3% for 10-15% helium [11–13]. Cosmogenic backgrounds associated with neutrons may be mitigated by a further addition of up to 5%  $^3\text{He}$  due to its high neutron capture cross section [14].

**Topology TPC:** Molecular additives such as  $\text{CO}_2$ ,  $\text{CH}_4$ ,  $\text{CF}_4$ , triethylamine (TEA:  $\text{N}(\text{CH}_2\text{CH}_3)_3$ ), and trimethylamine (TMA:  $\text{N}(\text{CH}_3)_3$ ) can be introduced to the TPC and significantly reduce the electron diffusion. This is by introducing new molecular degrees of freedom from vibrational and rotational states to transfer the electron energy in inelastic collisions [15]. This reduction enables finer resolutions to the charged particle tracks produced in the TPC and superior background rejection power at the analysis level compared with pure xenon.

These molecular gas additives, however, can also significantly change the TPC operation, whereby they can quench or absorb the VUV scintillation light. Furthermore, molecules such as and TMA can convert xenon excimers to ionization electrons through Penning transfers enabling higher avalanche gains and reduction of the Fano factor [16].

The use of such additives is considered to be more challenging to realize for a tonne-scale gas detector with further R&D required to establish suitable position reconstruction and sub-percent energy resolution with reduced/without electroluminescence. For example, at modest percentages with  $\text{CO}_2$  admixture, the EL can reduce to 70% or 35% compared with pure xenon for  $\text{CO}_2$  levels 0.05% and 0.1%, respectively [17, 18] with a reduction in the transverse diffusion by about a factor of three to four. At higher levels towards 5%, both longitudinal and transverse diffusion would reduce by a factor three to ten compared with pure xenon, respectively. However, this must be balanced with the strong quenching of scintillation light.

TMA with a few percent admixture has one of the strongest diffusion-reducing effects with electron diffusion coefficients,  $D_{L/T}^*$ , as low as  $0.3 \text{ mm}/\sqrt{\text{cm}} \times \sqrt{\text{bar}}$  [19]. The TPC would be operated with proportional avalanche signal amplification, and exploiting its strong Penning effect and fluorescence at  $\sim 280 \text{ nm}$  [20]. A useful estimate for the energy resolution with proportional avalanche gain can be obtained from an extrapolation of the resolution obtained with proportional counters filled with xenon and TEA (expected to behave similarly to TMA) [21]. In this work using a 22 keV  $^{106}\text{Cd}$  x-ray, an energy resolution of 8% FWHM was obtained. Extrapolating to 2.5 MeV with a  $1/\sqrt{\text{energy}}$  dependence (a factor of over 111) a resolution  $\sim 8/\sqrt{111} = 0.76\%$  FWHM is obtained. This assumes each electron is multiplied independently of others and with statistically equivalent early fluctuations. Further work with TMA-xenon gas have reported extrapolated resolutions of 1.2% FWHM at 1 bar with 30 keV x-ray source [19]. Higher energy calibration sources with MeV energy in TMA-xenon gas mixtures at low pressure are yet to be explored, while at high pressures towards 10 bar, worsening energy resolutions reaching 3% FWHM have been reported [22, 23].

Positional placement of events may utilize the use of the diffusion spread of the energy deposits or by measuring the positive ion signals that would drift to the cathode [24] and accounting for the drift time difference to the ionization, for example.

**Ion TPC:** Molecular additives can be introduced such that they capture ionization electrons or can undergo charge transfer with the ionized xenon [25]. The resulting ions

will drift to the cathode to be imaged with sub-mm diffusion over meter-scale drift lengths, allowing for almost diffusion-free tracking that would now be limited by the smallest pixelization achievable for the detector readout. Ion diffusion is not minimized at the same E/P as for electron diffusion, so optimization of the drift field should be considered in this mode. Similar to the Topology TPC operation, such detector technologies are a less well-explored domain, with potential losses to VUV scintillation light and detector fiducialization that must be considered.

### 2.3 Analysis Challenges

The overall intrinsic rate of background is coupled with the choices made in the detector design challenges discussed in Sec. 2.1. The major backgrounds that can deposit energy near the  $Q_{\beta\beta}$  include:

- Standard Model (SM) Double Beta Decay ( $2\nu\beta\beta$ ): This background produces two beta electrons where the summed energy of the betas is a continuous spectrum. This background is not considered in this work as it can be reduced to negligible levels with an energy resolution less than 1% FWHM.
- $^{214}\text{Bi}$ : The radioisotope  $^{214}\text{Bi}$  originates from the natural decay chain of  $^{238}\text{U}$ . This beta decays to  $^{214}\text{Po}$  that releases a number of deexcitation gammas to the ground state. One of these gammas has an energy of 2.448 MeV with branching fraction of 1.5%. The largest source of this background comes from the inner copper shielding which has trace amounts of  $^{238}\text{U}$  assumed to be in secular equilibrium with  $^{214}\text{Bi}$ . The 3.2 MeV beta from the decay  $^{214}\text{Bi}$  (branching fraction 19.2%) and the prompt (100  $\mu\text{s}$ ) 7.8 MeV  $\alpha$  from  $^{214}\text{Po}$  can also become a background if the decay is near the copper surface, referred to as *Bi-Po*.
- $^{208}\text{Tl}$ : The radioisotope  $^{208}\text{Tl}$  originates from the natural decay chain of  $^{232}\text{Th}$  with a branching fraction of 35.9%. This beta decays to  $^{208}\text{Pb}$  that releases a number of deexcitation gammas to the ground state. One of these gammas has an energy of 2.615 MeV with branching fraction of 99.8%. The largest source of this background also comes from the inner copper shielding which has trace amounts of  $^{232}\text{Th}$  assumed to be in secular equilibrium with  $^{208}\text{Tl}$ .
- Cosmogenic: The radioisotope  $^{137}\text{Xe}$  is produced from neutron capture on the source isotope  $^{136}\text{Xe}$  with neutrons originating predominantly from cosmogenic origin, such as muon spallation on the external rock. This isotope beta decays with a half-life of 3.8 minutes, producing a single electron with 4.17 MeV end-point energy in the gas volume. Neutrons can also activate materials such as the inner copper shielding, leading to a broad energy spectrum of gamma rays up to 8 MeV. These cosmogenic gamma backgrounds are prompt and can be suppressed to a sub-dominant level with a suitable muon rejection system with veto time  $\sim 2$  ms [26].
- Radon: The radon isotope  $^{222}\text{Rn}$  originates from the  $^{238}\text{U}$  decay chain with a half-life of 3.8 days. The isotope can diffuse into the gas volume, decaying through multiple

steps. About 95% of these decays result in a charged state of  $^{214}\text{Bi}$  that drifts to and plates out on the cathode. This results in an additional source of Bi-Po background correlated with the activity of  $^{222}\text{Rn}$ . Reduction of this background is assumed to be negligible, assuming a suitable position of the event along the drift direction [27]. The impact of this background without event placement is also investigated considering scenarios with a Topological/Ion TPC.

The requirement to reach sensitivities to the half-life beyond  $10^{27}$  years is to reduce these backgrounds to less than a fraction of a count per tonne of isotopic mass per year per a region of interest (ROI) energy window around the  $Q_{\beta\beta}$  (count/tonne/year/ROI).

This work separates the background rejection power as a function of three categories: (i) containment efficiency, (ii) energy resolution, and (iii) selection performance.

The containment efficiency describes the fraction of events that deposit energy near the  $Q_{\beta\beta}$  region and is predominantly affected by the choice of gas pressure and detector geometry. The optimal scenario is to have high signal containment and low background containment. We consider two scenarios: (i) a detector optimized for using xenon enriched in  $^{136}\text{Xe}$  to 90% and (ii) a detector that uses natural xenon which has about 9%  $^{136}\text{Xe}$ . A natural xenon detector may be employed to improve the signal containment efficiency and/or if obtaining enriched xenon is not feasible on the timescale of the detector construction. Furthermore, a natural xenon detector could be employed if initial operation is done at 1-tonne  $^{136}\text{Xe}$  mass and then the enrichment fraction is improved over time to include 5–10 tonnes of  $^{136}\text{Xe}$ .

The energy resolution of the experiment is strongly dependent on the method of signal amplification, such that the gain process is proportional to the initial number of ionization electrons. The most common method used in GXeTPC  $0\nu\beta\beta$  experiments such as NEXT and AXEL is via electroluminescence which have achieved resolutions near  $Q_{\beta\beta}$  in the range 0.7 – 0.9% FWHM [9, 10].

With the low-density of the xenon gas, MeV-scale electron tracks can travel about 30 cm at 10 bar. The selection performance with topological reconstruction of these tracks is powerful in identifying signal from background in GXeTPCs. The signature of signal events includes the identification of two electrons, while the backgrounds typically produce one electron tracks. These electrons scatter within the gas as they lose energy, near the end of the trajectory a large amount of energy is deposited known as a “blob” which can be used to identify the number of electrons in a track.

### 3 Detector Simulation and Geometry

The detector simulation uses a simple cylindrical geometry (diameter equal length) implemented in the open-source NEXUS framework, a Geant4 [28–30] based simulation framework developed by the NEXT collaboration [31]. The cylinder has a volume of xenon gas with gas pressure varied from 1, 5, 10, 15 and 25 bar. This volume is surrounded with a 4 cm layer of copper to model the inner copper shielding. This thickness was chosen since the simulation at 1 bar was prohibitively slow, and is normalized to give the expected rate assuming 12 cm copper shield.

The detector size is adjusted to account for changes in pressure to maintain 1 tonnes of  $^{136}\text{Xe}$  for either an enriched xenon detector (1-tonne module) or a natural xenon detector (10-tonne module). Table 1 details the simulated pressures and detector sizes, and Fig. 1 shows the total mass of copper shielding required for 12 cm thickness.

Pressure (bar)	Length (Enriched Xe) [m]	Length (Natural Xe) [m]
1	6.2	13.3
5	3.6	7.8
10	2.9	6.2
15	2.5	5.3
25	2.1	4.6

**Table 1.** Detector side-lengths at various pressures and enrichments. This assumes a cylindrical detector, with equal diameter to length and 1 tonne of  $^{136}\text{Xe}$ . The enriched assumes 90% enrichment and natural assumes 9% enrichment.

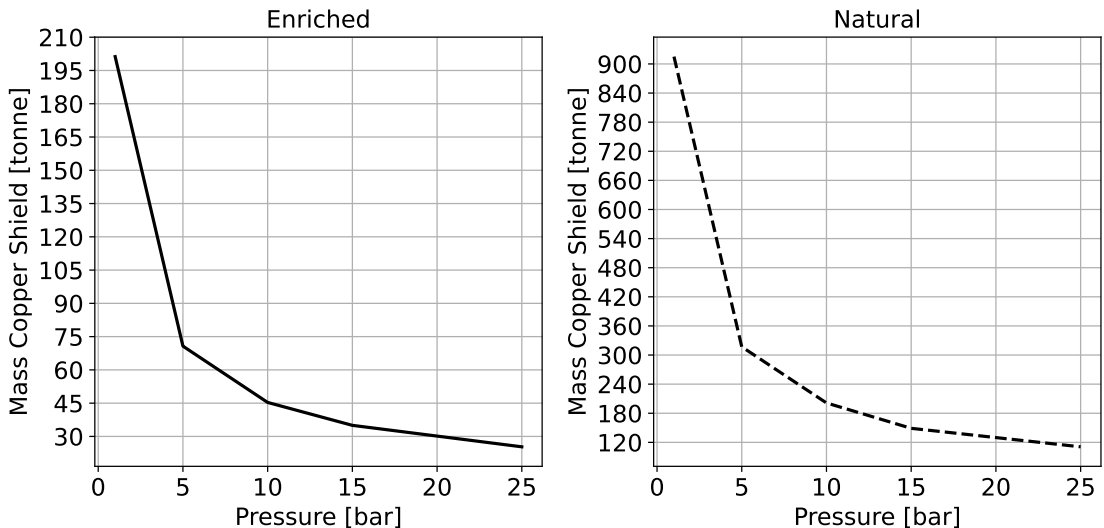


**Figure 1.** The total mass of inner shielding copper as a function of pressure for (left) enriched and (right) natural detector assuming 12 cm thickness.

Events are generated in the gas producing energy depositions (“hits”) along the track trajectory. For the  $0\nu\beta\beta$  decay and  $^{137}\text{Xe}$  backgrounds, events are generated directly in the gas volume. For the gamma backgrounds,  $^{214}\text{Bi}$  decays and  $^{208}\text{Tl}$  decays are generated in the 4 cm of copper surrounding the detector. The number of interacting events is scaled down by a normalization factor of 0.37, constant with pressure, to give rates corresponding to 12 cm of copper. This factor was derived from generating 100 million  $^{214}\text{Bi}/^{208}\text{Tl}$  decays in the different thicknesses of copper.

After generation, we save the information on the number of events depositing energy within a broad energy window of 2.3 – 2.6 MeV. An energy smearing, assuming 1% FWHM, is then applied to these events. In the next step, a filter saves full event information,

including energy deposits and particle information, only for events that deposit energy within 1% FWHM of the  $Q_{\beta\beta}$  value (2.43 - 2.48 MeV) in the gas region. This pre-selection saves on computational resources for the next reconstruction stage, and the choice of 1% FWHM energy resolution was to ensure there are sufficient statistics of events to analyze near the  $Q_{\beta\beta}$ . It is not expected that the topological signatures will vary for energy resolutions considered in this work ranging from 0.3–1.2% FWHM.

Different amounts of diffusion are then applied to smear the ionization electron positions based on a 3D Gaussian accounting for the longitudinal and transverse diffusion. The diffusion amounts considered are to model an EL TPCs (xenon-helium), Topology TPC (xenon- $\text{CO}_2$ ), and Ion TPC (no diffusion). Across all pressures, 10% He, 5%  $\text{CO}_2$ , and no diffusion are simulated. The use of a larger variation of gas additive percentages for  $\text{CO}_2$  allows for a slowly varying scan of different diffusions. Its application here can be extrapolated to other molecular additives, as described in Sec. 2.2, with similar reductions in diffusion, such as TMA. This finer diffusion scan is studied at 1 bar only.

The diffusion amounts are summarized in Table 2 assuming a reduced drift electric field of 60 V/cm/bar.

Gas Mix	$D_L^*$ ( $\sqrt{\text{bar}} \text{ mm}/\sqrt{\text{cm}}$ )	$D_T^*$ ( $\sqrt{\text{bar}} \text{ mm}/\sqrt{\text{cm}}$ )
Pure Xe	0.900	3.500
10% He	0.750	1.600
0.10% $\text{CO}_2$	1.307	0.818
0.25% $\text{CO}_2$	0.627	0.463
5.00% $\text{CO}_2$	0.314	0.300

**Table 2.** Longitudinal ( $D_L^*$ ) and Transverse ( $D_T^*$ ) diffusion coefficients as a function of  $\text{CO}_2$  percentage/helium at a drift electric field of 60 V/cm/bar. Diffusion values are calculated from PyBoltz [32] and with definitions in Ref. [13].

Given the large amount of ionization electrons ( $\sim 10^5$  produced for a 2.5 MeV track), a rebinning of the track into 3D voxels is applied with voxel sizes shown in Table 3. Voxelization also models a finite pixelization of a realistic detector. The choice of voxel sizes in millimeters is estimated based on the average of the transverse/longitudinal diffusion amount, pressure dependence on diffusion, and maximum drift distance, such that the voxel size is roughly the size of a maximally diffused track:

$$\text{voxel size} = \frac{D_L^* + D_T^*}{2} \times \frac{\sqrt{L[\text{cm}]}}{\sqrt{P}}, \quad (3.1)$$

where  $L$  is the maximum drift length in cm, and  $D_L^*/D_T^*$  are the longitudinal/transverse diffusion constants in  $[\sqrt{\text{bar}} \text{ mm}/\sqrt{\text{cm}}]$  as defined in Ref. [13]<sup>1</sup>. This also accounts for assuming a fixed  $E/P$  such that the drift field scales in proportion with pressure. The voxel sizes are rounded to the nearest integer except for the no diffusion sample. This sample uses non-integer bin sizes to try to preserve as much of the track detail as possible

<sup>1</sup>We note that another choice for the voxel size could account for the two transverse and one longitudinal degree of freedom:  $(D_L^* + 2D_T^*)/3$  or even voxels with different lengths in the drift and transverse directions.

while keeping file sizes manageable. We do not consider the impact of varying the voxel size on the performance.

An energy threshold of 300 eV is also applied to remove the low-energy diffuse hits around track edges after smearing and reduce the file sizes to a more manageable size. The energy of these removed hits is proportionally redistributed to the rest of the track and involves typically less than 0.5% of the total energy of the track.

<b>P [bar]</b>	<b>10% He [mm] (EL TPC)</b>	<b>5% CO<sub>2</sub> [mm] (Topology TPC)</b>	<b>No Diffusion [mm] (Ion TPC)</b>
1	29	8	5
5	10	3	2.2
10	6	2	1.6
15	5	1	1.3
25	3	1	1

**Table 3.** The voxel sizes used in the analysis for all pressures. A voxel size of 55, 23, and 15 mm was used for the pure xenon, 0.1% CO<sub>2</sub>, and 0.25% CO<sub>2</sub>, respectively. These additional diffusion values are studied for 1 bar pressure only.

The final event samples contain roughly 200k events for each background category within a window of 1% FWHM of the signal peak (2.43–2.48 MeV). Examples of signal events with 5% CO<sub>2</sub> and 10% He are shown in Fig. 2. The visualization shows all the included hits, adding a coarse sharpness to track edges.

## 4 Analysis

As described in Sec. 2.3, the analysis stages can be broken down into three stages. For each stage, we define the acceptance factor,  $\eta$ , which is defined as the number of events selected divided by the total number of events in the initial or sub-sample. The total acceptance factor is then given by:

$$\eta = \eta^{\text{cont}} \times \eta^{\text{Eres}} \times \eta^{\text{sel}}, \quad (4.1)$$

where  $\eta^{\text{cont}}$  is the containment efficiency,  $\eta^{\text{Eres}}$  is the selection efficiency after applying an energy resolution cut, and  $\eta^{\text{sel}}$  is the selection efficiency using event topology cuts.

### 4.1 Containment Efficiencies

The event containment as a function of pressure for the signal and backgrounds and for an enriched and natural detector geometry is shown in Fig. 3. The containments are defined by the number events depositing 2.3–2.6 MeV in the gas volume divided by the total decays simulated. This range is chosen to allow a better understanding of the impact of energy resolution.

The signal events and <sup>137</sup>Xe follow a similar trend. This is due to the similarities of the events of either one or two beta electrons being produced in the gas volume. The containment is a factor 10 lower for the <sup>137</sup>Xe background compared with the signal because

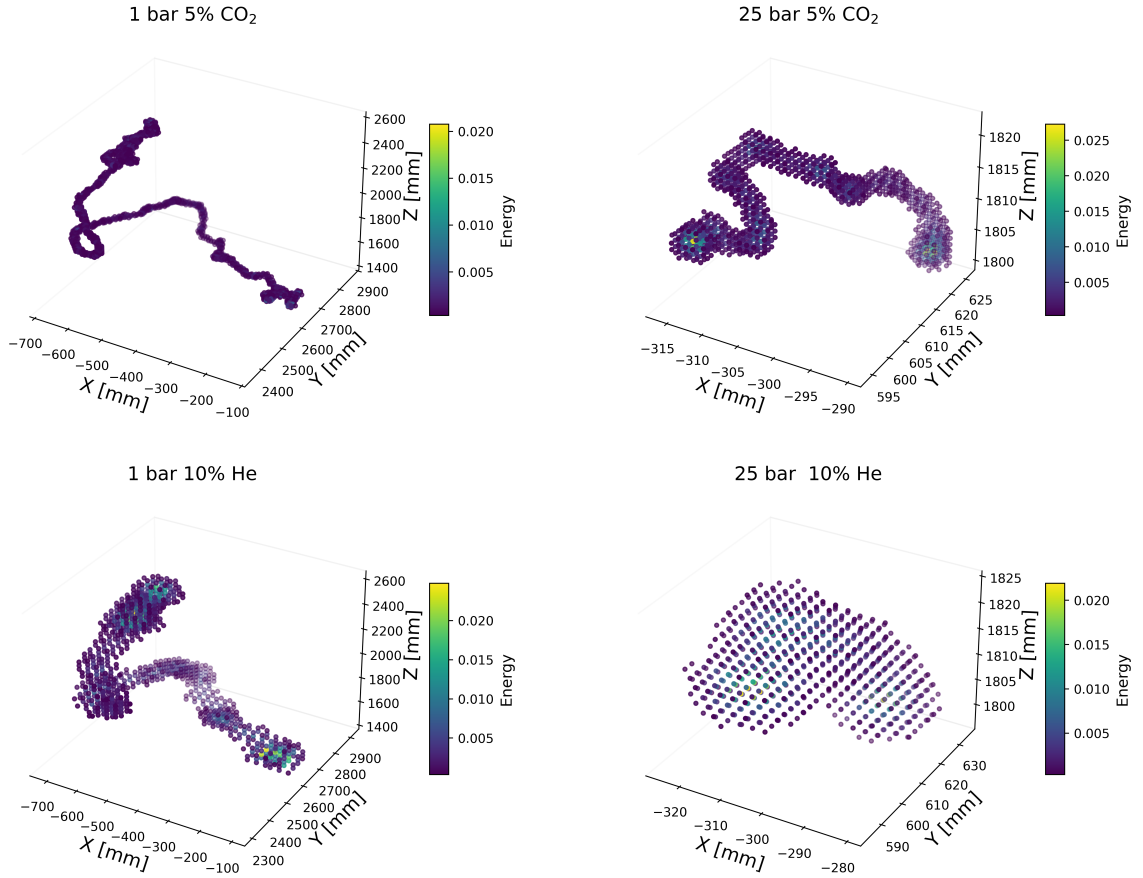


**Figure 2.** Example of the same signal event with different amounts of diffusion applied at 1 bar and 25 bar. These events include a 300 eV energy threshold.

across the whole beta decay spectrum for this background, only about 9% of betas will have an energy between 2.3–2.6 MeV.

The signal efficiency varies rapidly from 1 to 5 bar, with only 60% of events contained at 1 bar, whilst it is 80-90% for pressures above this. Lower signal containment efficiency reduces the strength that following analysis cuts can make due to the lower number of signal events. A natural xenon detector size has a larger volume, which increases the overall containment of the signal and background at lower pressure.

At lower pressures, gamma backgrounds are effectively screened due to the lower cross section of interaction in the gas, leading to the lower containment fractions. However, interestingly, the  $^{214}\text{Bi}$  and  $^{208}\text{Tl}$  have a different shape with increasing pressure. The event distribution within the 2.3–2.6 MeV window can be seen in Fig. 4, top left. The majority of events from  $^{214}\text{Bi}$  consist of the photopeak of a 2.448 MeV gamma ray, while the majority of events from  $^{208}\text{Tl}$  consist of single and multiple Compton scatters of a 2.615 MeV gamma ray.

The highest probability interaction mode of the  $\sim$ 2.5 MeV gamma rays is via Compton scattering, occurring for about 80% of all initial interactions. This initial scatter results

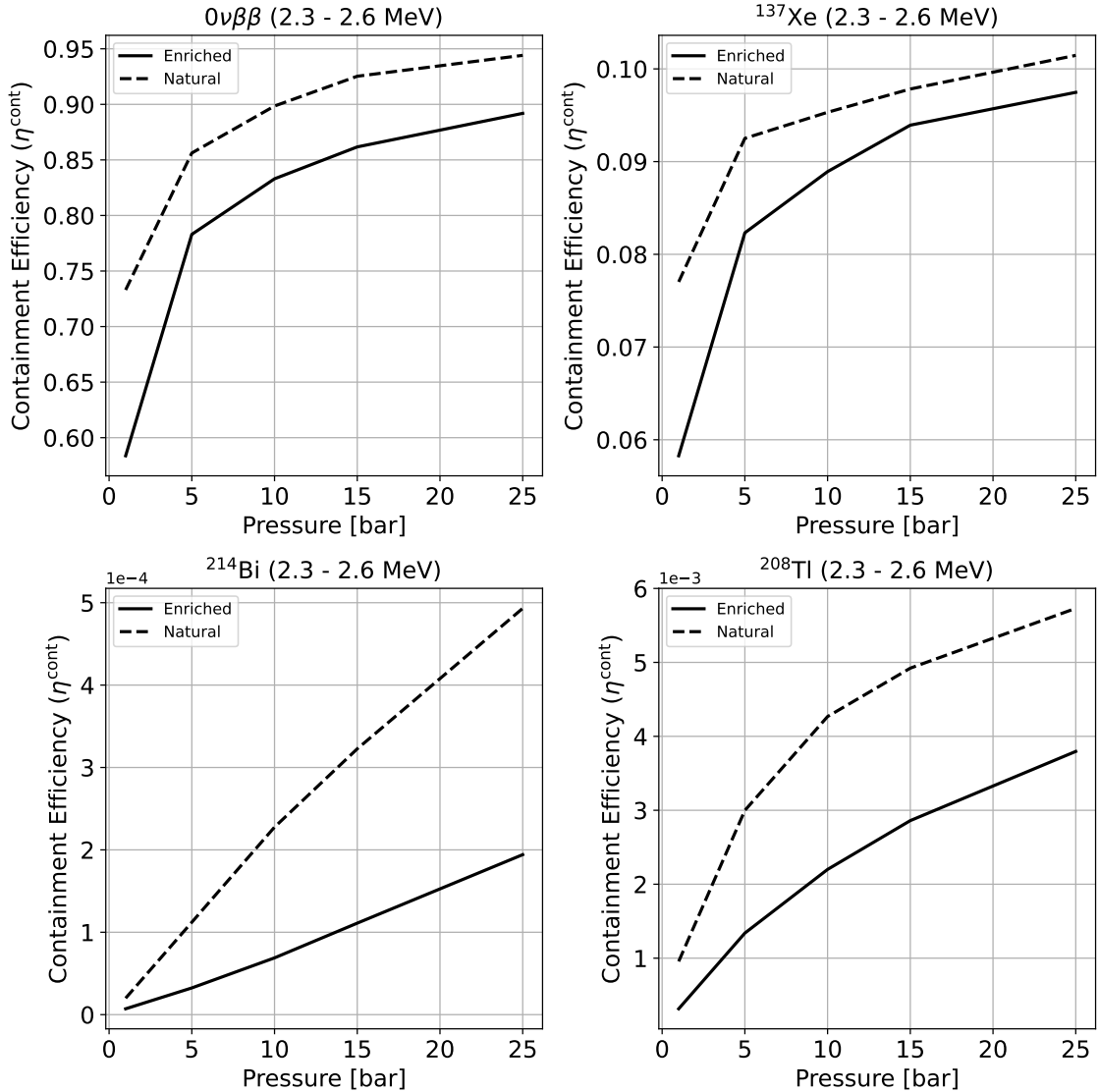


**Figure 3.** The fraction of events depositing energy within 2.3–2.6 MeV of energy to the number of decays of each radioisotope for an enriched and natural detector size.

in a second lower-energy gamma. For  $^{214}\text{Bi}$  events, this daughter gamma needs to deposit nearly all of its energy in the gas volume leading to the photopeak in the 2.3–2.6 MeV window. In the case of  $^{208}\text{Tl}$ , this gamma must re-interact but only deposit part of its energy in the gas volume as the energy window is below the photopeak of this gamma. At higher pressure, the partial energy deposition of the low-energy gamma is less likely compared to full energy deposition, and this effectively reduces the interaction rate at higher pressure.

Overall, lower pressures are favorable for reducing the gamma backgrounds where 1 bar has almost a factor 10 and 30 lower containment compared to 25 bar for  $^{208}\text{Tl}$  and  $^{214}\text{Bi}$ , respectively. For all event categories, the containment fractions increase when going

from an enriched to a natural detector size.

## 4.2 Energy Resolution

The detector energy resolution is important for reducing the  $2\nu\beta\beta$  backgrounds to negligible levels, and is also powerful in significantly reducing the other backgrounds. Fig. 4, top left, shows the distributions assuming a 0.5% FWHM energy resolution. The dashed vertical lines mark around the signal peak shown in grey one FWHM at 0.5% resolution corresponding to a ROI of 2.45–2.47 MeV.

The  $^{137}\text{Xe}$  backgrounds are flat across this energy range, while the  $^{208}\text{Tl}$  has a slowly decreasing slope. The bump at  $\sim$ 2.37 MeV corresponds to the Compton edge of the 2.615 MeV gamma ray. The  $^{214}\text{Bi}$  background includes the photopeak of the 2.448 MeV gamma along with a few higher energy  $^{214}\text{Po}$  deexcitation gammas.

A lower energy resolution increases the width of Gaussian smear applied to these distributions allowing more events to overlap with the signal. The overall acceptance of background is shown in Fig. 4, top right and bottom row for each background for different energy resolutions assumed ranging from 0.3% FWHM to 1.2% FWHM for events depositing an initial energy within 2.3–2.6 MeV. The 0.3% represents the intrinsic resolution of a GXeTPC from Fano fluctuations [16] assuming energy is measured from the ionization charge, while 1.2% energy resolution represents a less-favorable detector energy resolution. The more realistic energy resolutions are in the range 0.5% to 1% FWHM. These distributions were generated assuming 25 bar pressure; however, the shape of these distributions is not expected to significantly vary with pressure.

The distributions are plotted as a function of a relative signal efficiency loss obtained from applying an asymmetric cut in the ROI. This cut is done by increasing the value of the lower bound energy range in the ROI window. This is better visualized by considering Fig. 4 top left, whereby the dashed blue line is moved to the right. As this cut value is increased, this causes the total signal efficiency to reduce while also rejecting more background.

The shape of the energy resolution curves are similar for  $^{137}\text{Xe}$  and  $^{208}\text{Tl}$  backgrounds as their shape is mostly flat while there is a stronger slope with  $^{214}\text{Bi}$  due to the variation of the energy cut along the photopeak.

## 4.3 Reconstruction

Following the containment and energy resolution, the last stage in the analysis is to apply a selection to utilize the topology of the tracks.

An initial fiducial volume is applied to all events, such that if any hit falls within 2 cm of the detector wall then it is rejected. This is particularly effective in removing the Bi-Po backgrounds.

The reconstruction algorithm then builds tracks out of the energy-weighted center of diffused hits that are within a given proximity. The track consists of a set of contiguous points falling in a line. Some interactions may have multiple separated tracks, for example, when a gamma ray undergoes multiple Compton scatters or a  $0\nu\beta\beta$  beta electron emits bremsstrahlung radiation that then deposits energy away from the main track.

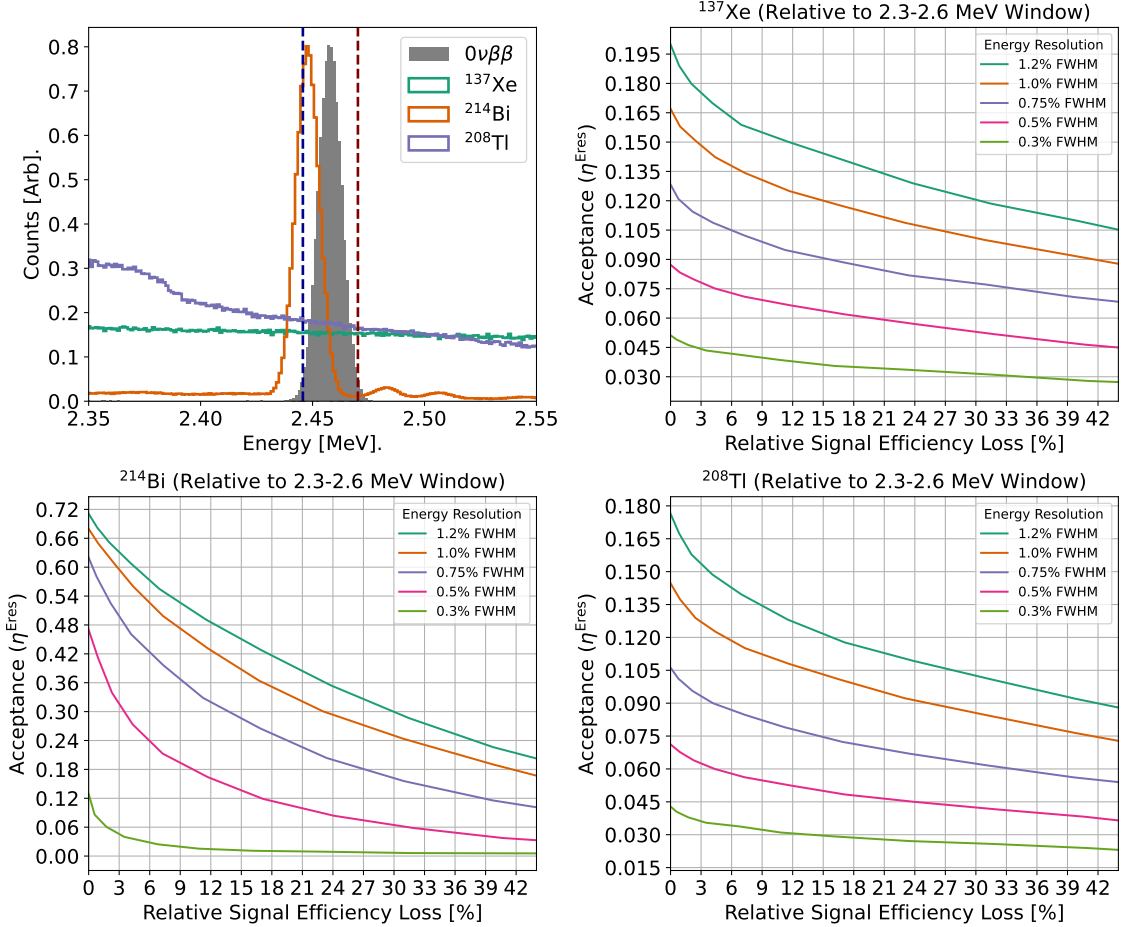


**Figure 4.** Top left: The distributions of background assuming 0.5% FWHM energy resolution. The blue and maroon dashed lines represent the bounds of one 0.5% FWHM window. An asymmetric cut is done on this window by increasing the lower bound (blue line). Top right, bottom left, bottom right, show the background acceptance rates assuming different energy resolutions for  $^{137}\text{Xe}$ ,  $^{214}\text{Bi}$ ,  $^{208}\text{Tl}$ , respectively. The x-axis shows the efficiency loss vs background acceptance from increasing the lower bound cut on energy.

The primary track is defined as the track with the largest energy. In some cases, the electron may produce high energy delta electrons forking the track into three or more branches. In these cases, the primary track and information associated with this is defined as the longest segment from two end-points on the track.

We extract several variables from the primary track, including its total energy and length. One of the most effective variables is the “blob energy” which integrates the total energy in a sphere of radius  $r$  around the track start and end. Blob 1 is defined as the blob with the highest energy, with blob 2 being the lowest energy blob. This variable is a key marker in identifying an electron stopping in the gas. Applying a minimum threshold to the blob 2 energy can remove a significant number of the gamma and  $^{137}\text{Xe}$  backgrounds as the track start of these single electron-like backgrounds does not produce a distinct blob.

The primary track energy and length are effective at removing events with significant bremsstrahlung and also multi-site interactions, as this reduces the overall primary track energy. It is effective to employ a single track cut to remove these multi-site events; however, this work opts to use the primary track information. This is because at 1 bar the single track cut leads to a 54% signal efficiency loss when applied to the no diffusion and 5% CO<sub>2</sub> samples and this results in a final efficiency below 25%. This is due to a higher efficiency of tagging separated deposits near the track from bremsstrahlung. A separate analysis optimization was done for 5–25 bar employing a single track cut, and no significant difference in the overall performance was found using either method.

The overall selection is optimized such that the final signal efficiency is about 25% for all pressures and diffusions considered so they can be consistently compared. This final efficiency includes the containment efficiency and an assumed energy resolution of 0.75% with an asymmetric cut with 18% relative efficiency loss corresponding to an ROI of 2.451–2.476 MeV.

#### 4.4 Selection Diffusion Dependence

To investigate the selection performance with diffusion, we consider 1 bar pressure scanning over a range of diffusion values listed in Table 2. We also show the dependence as a function of a mean diffusion coefficient,  $\bar{D}^* = (D_L^* + D_T^*)/2$  for reference. The selection acceptance factors are shown in Fig. 5, considering an enriched and natural detector configuration.

For an enriched detector, there is about a factor of three to four reduction in background rejection power when using pure xenon compared with gas mixtures that reduce diffusion. The improvement with decreasing diffusion is expected since the overall track clarity and reconstruction of track information are improved.

A natural detector has a similar trend to enriched and offers about a factor of two improvement in the overall selection power at 1 bar. This is primarily due to the higher signal containment efficiency, where stronger analysis cuts can be applied.

#### 4.5 Selection Pressure Dependence

The acceptance factor for each background and across different pressures for an enriched detector is shown in Figure 6, considering the diffusions for 10% He, 5% CO<sub>2</sub>, and no diffusion. Background rejection ranges from 90–99.9% depending on the background category.

Of the remaining backgrounds, the most frequent cases consist of topologies where a high energy delta electron is produced near the track start or gamma ray interactions produced from bremsstrahlung or Compton scatters deposit energy near the track start. Both of these signatures produce a stopping electron near the track that mimics a two-electron  $0\nu\beta\beta$  event signature. The most difficult backgrounds to reduce are the <sup>137</sup>Xe, while the best background rejection is obtained for <sup>208</sup>Tl events. This difference in performance is due to the subtle differences in topologies for how these backgrounds deposit energy in the ROI. <sup>208</sup>Tl tends to have more multi-track topologies due to multiple gamma interactions while selected <sup>137</sup>Xe background topologies have a higher fraction of topologies containing a high energy delta ray occurring near the track start. <sup>214</sup>Bi sits between these two backgrounds as its photopeak is similar to producing a single electron in the ROI, like

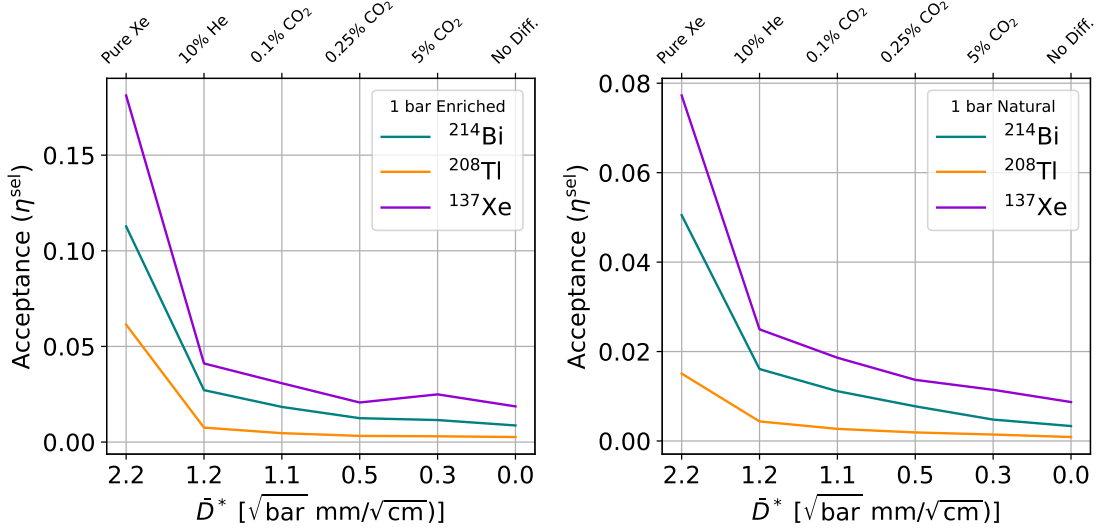


**Figure 5.** Background acceptance factors for voxelized tracks at 1 bar for different diffusion amounts for an enriched (left) and natural (right) detector configuration. Overall, the dependence on diffusion has a similar functional form.

$^{137}\text{Xe}$  backgrounds, while it can also deposit energy in the ROI through multiple gamma interactions, like  $^{208}\text{Tl}$ .

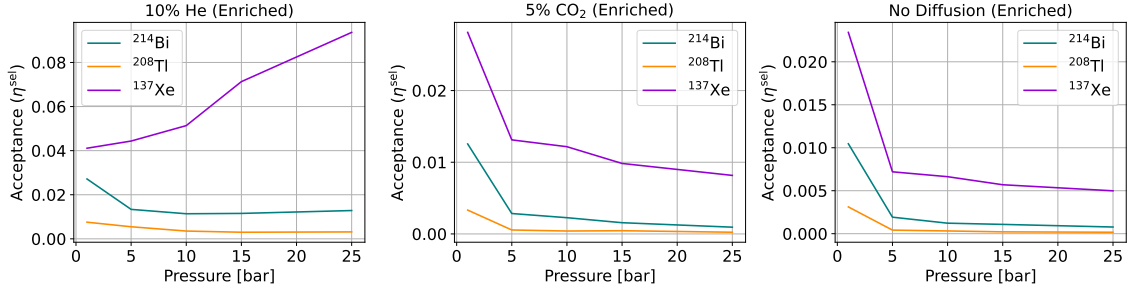


**Figure 6.** The acceptance factors from the topological selection for different diffusion amounts as a function of pressure.

For the 10% He sample, performance reduces with increasing pressure for the  $^{137}\text{Xe}$  background while  $^{208}\text{Tl}$  and  $^{214}\text{Bi}$  performance improves with pressure. This difference in background rejection with pressure is due to the worsening track reconstruction of the primary track with larger pressures, affecting variables that are harder to reconstruct such as the blob energy. The  $^{137}\text{Xe}$  background is more affected by this worsening performance as these backgrounds rely more on the blob information while gamma backgrounds can be rejected more efficiently using more handles such as the total primary track energy and single track vs multi track topologies.

Similar to the 1 bar case, the overall performance improves with reducing the diffusion amount across higher pressures. In the case of the 5% CO<sub>2</sub> and no diffusion all backgrounds

show the same behavior of improved performance with pressure, due to the better quality of track reconstruction.

## 5 Results

This section presents the overall acceptance factor and rates. We start with showing how the acceptance factors and rates change from events depositing energy in a 2.3 – 2.6 MeV energy window to the final selection for an enriched detector scanning the diffusion amount and pressure at a fixed energy resolution of 0.75% FWHM. Following this, the total rates are shown as a function of energy resolution for different assumed detector technologies.

### 5.1 Acceptance and Rate with Diffusion and Pressure

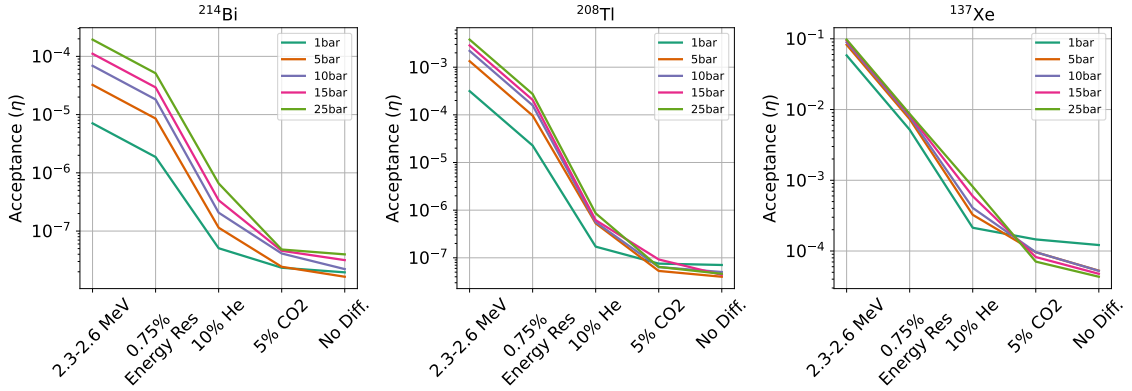


**Figure 7.** The total acceptance factors for each background category as a function of the analysis stage for an enriched detector configuration.

The total acceptance factor for an enriched detector as a function of the analysis stage for each pressure and background category is shown in Fig. 7. The performance of a natural detector can be found in Appendix A. Overall acceptance factors range from  $10^{-7}$ – $10^{-8}$  for  $^{208}\text{Tl}$  and  $^{214}\text{Bi}$  while  $^{237}\text{Xe}$  acceptance factor is around  $10^{-4}$ .

The acceptance factors can be used to estimate the overall background rate per tonne-year:

$$\text{Rate} = \frac{\eta \cdot A \cdot 3.15 \times 10^7}{M_{\text{Xe}}}, \quad (5.1)$$

where  $\eta$  is the total acceptance factor,  $A$  is the total radioactivity in Bq,  $3.15 \times 10^7$  is the number of seconds in a year, and  $M_{\text{Xe}}$  is the mass of  $^{136}\text{Xe}$  in tonnes. The activity factors in the total mass of copper for  $^{214}\text{Bi}$  and  $^{208}\text{Tl}$  or total mass of  $^{136}\text{Xe}$  for  $^{137}\text{Xe}$ .

For this work, we consider an activity of  $^{238}\text{U}$  and  $^{232}\text{Th}$  of 1.28 and 1.22  $\mu\text{Bq}/\text{kg}$ , respectively. The  $^{137}\text{Xe}$  assumes a site location at SNOLAB ( $\sim$ 6000 m water equivalent (w.e.) depth) and a water shield surrounding the detector to reduce the neutron flux, amounting to a total activity of  $\sim$ 1 count per year. A site location at LNGS ( $\sim$ 3400 m

w.e.) would increase the rate by a factor 100, and at LSC (2200 m w.e.) by a factor 1000 [14].

The rates for an enriched detector as a function of analysis stage are shown in Fig. 8. The overall rates are below 0.1 counts/tonne/year/ROI for all pressures and backgrounds except 1 bar for  $^{214}\text{Bi}$  and  $^{208}\text{Tl}$ . The lower performance at 1 bar is due to the increased mass of copper and lower signal containment efficiency. The  $^{137}\text{Xe}$  rate follows the same trend as the acceptance, as the total intrinsic activity depends on the fixed isotopic mass of  $^{136}\text{Xe}$ .

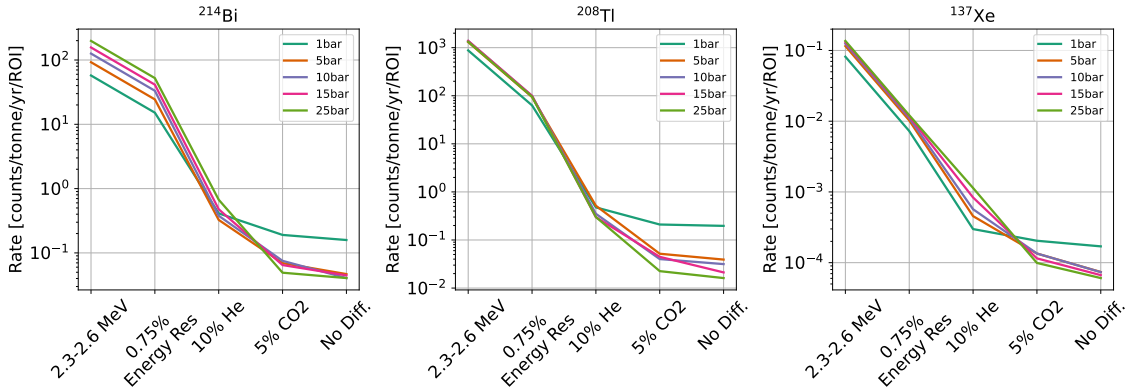


**Figure 8.** The total background rate for each background category as a function of the analysis stage for an enriched detector configuration.

## 5.2 EL TPC

A summary of the summed background rates for an EL TPC assuming 10% He gas admixture is shown in Fig. 9. These rates are summed over  $^{214}\text{Bi}$ ,  $^{208}\text{Tl}$ , and  $^{137}\text{Xe}$  and consider an enriched and natural detector scanning the different assumed energy resolutions and pressures. Overall, the rates with pressure are mostly flat with a more optimal value around 10 bar pressure.

For the enriched EL TPC, background rates are below 1 count/tonne/year/ROI for energy resolutions below 0.75% FWHM. Scanning across these varied energy resolutions can change the total rate by up to a factor of eight. A 0.5% FWHM energy resolution is feasible with this technology yielding a total rate of 0.5 count/tonne/year/ROI for a one-tonne module.

For the natural detector configuration, background rates are about a factor of 5 larger than those of the enriched detector. Rates similarly span a factor of eight across each energy resolution assumed.

## 5.3 Topology TPC

In the case of a Topology TPC, we assume a 5% CO<sub>2</sub> gas admixture to model the reduction in diffusion with a molecular gas additive. A summary of the summed background rates in this detector configuration, summed over  $^{214}\text{Bi}$ ,  $^{208}\text{Tl}$ , and  $^{137}\text{Xe}$ , is shown in Fig. 10.

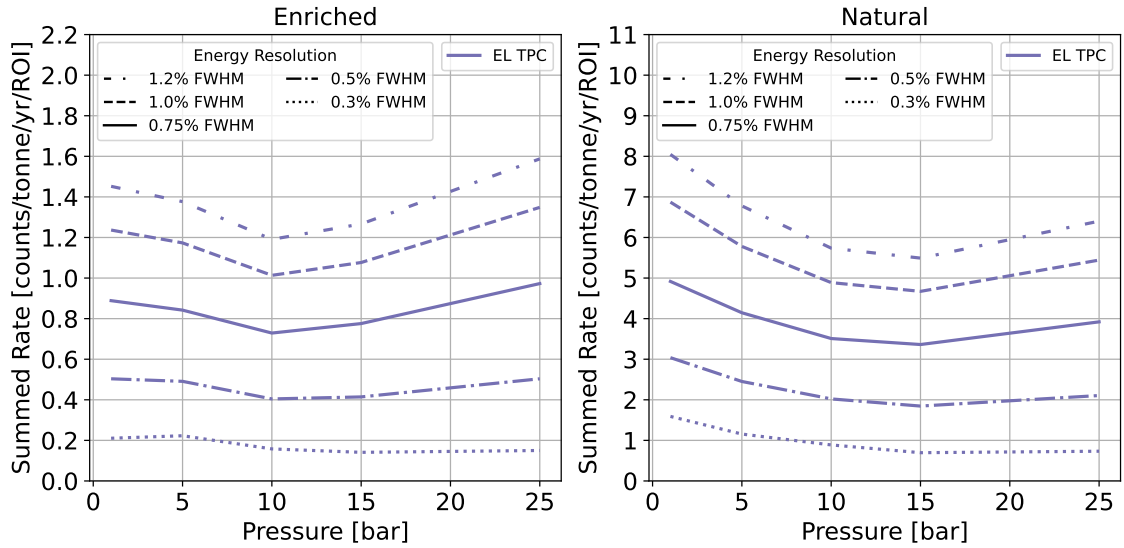


**Figure 9.** A summary of the summed background rate for an EL TPC including  $^{214}\text{Bi}$ ,  $^{208}\text{Tl}$ , and  $^{136}\text{Xe}$ . The left figure shows the performance for an enriched detector configuration, while the right figure shows a natural detector configuration.

These rates are for an enriched and natural detector scanning the different assumed energy resolutions and pressures.

Overall, the rates decrease with increasing pressure. Background levels just below 0.2 count/tonne/year/ROI are achieved for pressures greater than 5 bar. Similar to the EL TPC, the natural detector has a larger rate, reaching values below 1 count/tonne/year/ROI for pressures greater than 5 bar.

As commented on in Sec. 2.2, these performances assume the optimistic scenario where resolutions of at least 1.2% FWHM are achieved and a fiducial volume cut can be applied with similar power to an EL TPC. We investigate the impact of removing the fiducial volume cut on these rates and radon backgrounds in Appendix B. For the backgrounds originating from the detector surface, this introduces an increase in rate of about 0.1 counts/tonne/year/ROI, depending on the gas pressure and mixture. Background rates introduced from radon without suitable event placement would need to employ more advanced analysis techniques or explore new avenues for event vertex placement without VUV light to sufficiently tag the Bi-Po backgrounds.

#### 5.4 Ion TPC

In the case of an Ion TPC, we assume no diffusion. A summary of the summed background rates in this detector configuration (over  $^{214}\text{Bi}$ ,  $^{208}\text{Tl}$ , and  $^{137}\text{Xe}$ ) is shown in Fig. 11. These rates are for an enriched and natural detector scanning the different assumed energy resolutions and pressures.

The dependence and overall rates are similar to the Topology TPC. Likewise, these performances assume that such energy resolutions and suitable event placement are achieved.

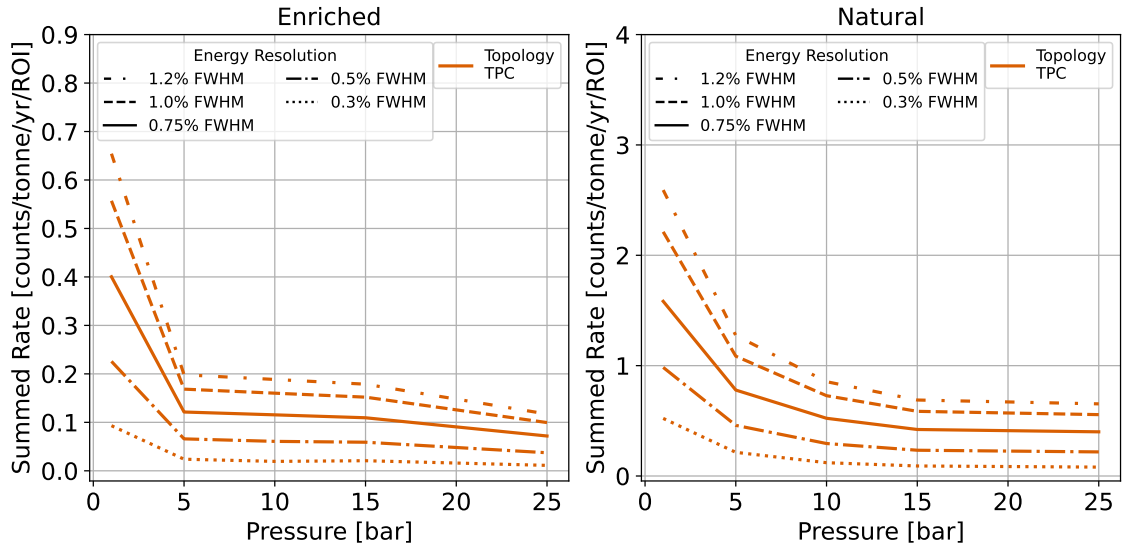


**Figure 10.** A summary of the summed background rate including  $^{214}\text{Bi}$ ,  $^{208}\text{Tl}$ , and  $^{136}\text{Xe}$ , for a Topology TPC modeled with 5%  $\text{CO}_2$  gas additive. The left figure shows the performance for an enriched detector configuration, while the right figure shows a natural detector configuration.

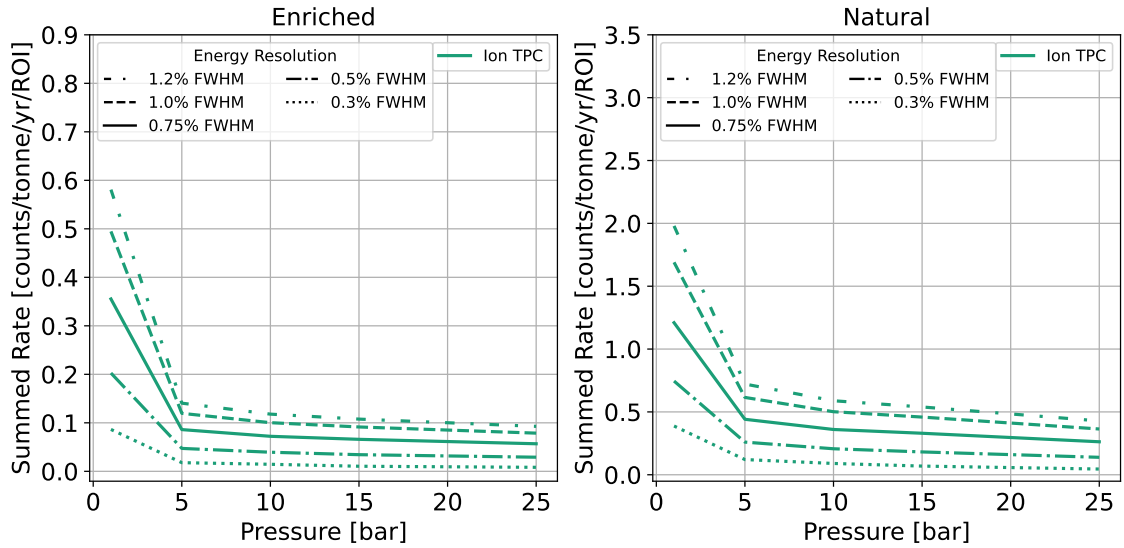


**Figure 11.** A summary of the summed background rate including  $^{214}\text{Bi}$ ,  $^{208}\text{Tl}$ , and  $^{136}\text{Xe}$ , for an Ion TPC. The left figure shows the performance for an enriched detector configuration, while the right figure shows a natural detector configuration.

## 6 Discussion and Summary

One of the major limitations of the natural detector configuration is the large mass of copper required to build a detector of that size. The possibility of operating the natural detector with 5–10 tonnes of  $^{136}\text{Xe}$  could help boost the signal-to-background ratio to yield

a similar performance to the enriched scenario. In this case, the  $^{137}\text{Xe}$  backgrounds would also increase proportionally to the  $^{136}\text{Xe}$  mass; however, this could be tolerated at a site such as SNOLAB, resulting in a rate below a fraction of a count/tonne/year/ROI. Similarly, the 1 bar suffers from the same issue of large copper mass and low signal containment efficiency. New engineering solutions to mitigate the copper background, and/or more effective analysis selections utilizing the higher track clarity should be explored in this detector configuration.

For pressures above 5 bar, the total background rates are flat. A further option would be to operate an enriched detector at 5 bar and then load in more isotope with increased pressure to pack in more source isotope. Detector design should optimize sensor readout and vessel design for the highest pressure planned to ensure suitable track clarity is maintained.

This work also considers a simple analysis for topological rejection in order to scan many parameters. Machine learning methods, which can account for the full topology of the track rather than using the end-point information, have been shown to further improve performance with respect to a simple analysis [33, 34] with potential for also improving signal efficiency. Furthermore, post-processing methods to reduce the effect of track blurring due to diffusion, such as deconvolution, have shown significantly improved background rejection performance [35]. The largest scope for improvement with more advanced reconstruction methods is at lower pressures, which can utilize the higher track detail to better reject backgrounds, such as identifying energetic delta rays occurring near the track start or tagging of atomic x-rays (K,L-shell) from photoelectric conversions from gamma-induced backgrounds.

In summary, this work investigates how the possible design choices can impact a gaseous xenon TPC searching for  $0\nu\beta\beta$  towards a half-life sensitivity of  $10^{27}$ – $10^{28}$  years considering a detector with one tonne of source isotope. We consider three of the major sources of background for the experiment arising from  $^{137}\text{Xe}$ ,  $^{214}\text{Bi}$ , and  $^{208}\text{Tl}$  radioactive decays. Several variables are surveyed, including detector size accounting for gas enrichment, copper shielding mass, gas pressure, energy resolution, and analysis performance. A detector configuration optimized for accommodating xenon enriched with  $^{136}\text{Xe}$  at 90% is preferred over operation with natural xenon with an order of magnitude lower background rate. This is due to the increase in intrinsic background due to the larger detector size and inner copper shielding mass, which overcomes the improvement in signal containment efficiency and analysis-level rejection power.

The performance of three gas TPC technologies was also explored based on different gas additives used to reduce diffusion. An EL TPC includes 10% helium preserving electroluminescence signals based on the well-established NEXT experiment detector design. The total rate is expected to be below 0.5 counts/tonne/year/ROI, assuming an energy resolution of 0.5% FWHM. The Topology and Ion TPCs include the addition of stronger diffusion-reducing molecular additives and could produce background rates below 0.2 counts/tonne/year/ROI. Such performances are contingent on a suitable event placement and energy resolution of better than 1.2% FWHM being achieved without the use of VUV light signals which may be quenched.

In addition to the analysis level performance, the construction of the detector is also highly dependent on gas pressure, influencing several factors including the intrinsic background rate, site location, gas containment, and detector size. Overall, there is no clear optimum pressure, with advantages and disadvantages if a high or low pressure default configuration is chosen.

## Acknowledgments

The authors would like to thank Ben Jones, Adam Para, Juan José Gomez Cadenas, Pau Novella, and Michel Sorel for their valuable feedback on this manuscript. This research used services provided by the OSG Consortium [36–39], which is supported by the National Science Foundation awards #2030508 and #1836650. We also acknowledge support from the following agencies: DE-SC0019054 (Texas Arlington) and DE-SC0019223 (Texas Arlington).

## References

- [1] S. Abe et al., *Search for Majorana neutrinos with the complete KamLAND-Zen dataset*, *Phys. Rev. Lett.* (2025) .
- [2] LEGEND collaboration, *First Results on the Search for Lepton Number Violating Neutrinoless Double Beta Decay with the LEGEND-200 Experiment*, *Phys. Rev. Lett.* (2025) .
- [3] NEXT collaboration, *The NEXT-100 Detector*, [2505.17848](#).
- [4] NEXT collaboration, *Design, characterization and installation of the NEXT-100 cathode and electroluminescence regions*, *JINST* **19** (2024) P02007.
- [5] NEXT collaboration, *High Voltage Delivery and Distribution for the NEXT-100 Time Projection Chamber*, [2505.01002](#).
- [6] L. Baudis, J. Hall, K.T. Lesko and J.L. Orrell, *Snowmass 2021 Underground Facilities and Infrastructure Overview Topical Report*, [2212.07037](#).
- [7] NEXT collaboration, *Sensitivity of a tonne-scale NEXT detector for neutrinoless double-beta decay searches*, *Journal of High Energy Physics* **2021** (2021) .
- [8] NEXT collaboration, *Reconstructing neutrinoless double beta decay event kinematics in a xenon gas detector with vertex tagging*, *Journal of High Energy Physics* **2025** (2025) 170.
- [9] AXEL collaboration, *AXEL: High-pressure xenon gas TPC for neutrinoless double beta decay with A Xenon ElectroLuminescence*, *Nuclear Instruments and Methods in Physics Research Section A* **1080** (2025) .
- [10] NEXT collaboration, *Energy calibration of the NEXT-White detector with 1% resolution near  $Q_{\beta\beta}$  of  $^{136}\text{Xe}$* , *Journal of High Energy Physics* **2019** (2019) .
- [11] NEXT collaboration, *Low-diffusion Xe-He gas mixtures for rare-event detection: Electroluminescence Yield*, *Journal of High Energy Physics* **04** (2020) 034.
- [12] NEXT collaboration, *Helium–Xenon mixtures to improve the topological signature in high pressure xenon TPCs*, *Nuclear Instruments and Methods in Physics Research Section A* **925** (2019) 294.

- [13] A.D. McDonald et al., *Electron drift and longitudinal diffusion in high pressure xenon–helium gas mixtures*, *J. Instrum.* **14** (2019) P08009.
- [14] NEXT collaboration, *Mitigation of backgrounds from cosmogenic  $^{137}\text{Xe}$  in xenon gas experiments using  $^3\text{He}$  neutron capture*, *Journal of Physics G: Nuclear and Particle Physics* **47** (2020) 075001.
- [15] C.D.R. Azevedo et al., *An homeopathic cure to pure Xenon large diffusion*, *J. Instrum.* **11** (2016) C02007.
- [16] U. Fano, *Ionization Yield of Radiations. II. The Fluctuations of the Number of Ions*, *Phys. Rev.* **72** (1947) 26.
- [17] NEXT collaboration, *Secondary scintillation yield of xenon with sub-percent  $\text{CO}_2$  admixtures*, *Physics Letters B* **771** (2017) 264.
- [18] NEXT collaboration, *Electroluminescence TPCs at the thermal diffusion limit*, *Journal of High Energy Physics* (2019) 027.
- [19] NEXT collaboration, *Characterization of a medium size Xe/TMA TPC instrumented with microbulk Micromegas, using low-energy  $\gamma$ -rays*, *Journal of Instrumentation* **9** (2014) C04015.
- [20] D. Nygren, *Can the “intrinsic” energy resolution in xenon be surpassed?*, *Journal of Physics: Conference Series* **309** (2011) 012006.
- [21] B. Ramsey and P. Agrawal, *Study of Argon-Based Penning Gas Mixtures for use in Proportional Counters*, *Nuclear Instruments and Methods in Physics Research Section A* **A278** (1989) 675.
- [22] PANDAX-III collaboration, *PandaX-III: Searching for Neutrinoless Double Beta Decay with High Pressure  $^{136}\text{Xe}$  Gas Time Projection Chambers*, [1610.08883](https://arxiv.org/abs/1610.08883).
- [23] D. González-Díaz et al., *Accurate  $\gamma$  and MeV-electron track reconstruction with an ultra-low diffusion Xenon/TMA TPC at 10 atm*, *Nuclear Instruments and Methods in Physics Research Section A* **804** (2015) 8.
- [24] P. Luke, *Unipolar charge sensing with coplanar electrodes-application to semiconductor detectors*, *IEEE Transactions on Nuclear Science* **42** (1995) 207.
- [25] D.R. Nygren, *A negative-ion TPC with ultra-high energy resolution for  $0\nu$  double beta decay search in  $^{136}\text{Xe}$* , *Journal of Physics: Conference Series* **65** (2007) 012003.
- [26] NEXT collaboration, *Demonstration of neutrinoless double beta decay searches in gaseous xenon with NEXT*, *Journal of High Energy Physics* **2023** (2023) .
- [27] NEXT collaboration, *Measurement of radon-induced backgrounds in the NEXT double beta decay experiment*, *Journal of High Energy Physics* **2018** (2018) 112.
- [28] J. Allison et al., *Recent developments in Geant4*, *Nucl. Inst. and Meth. in Phys. Res. Sect. A* **835** (2016) 186.
- [29] J. Allison et al., *Geant4 developments and applications*, *IEEE Trans. Nucl. Sci.* **53** (2006) 270.
- [30] S. Agostinelli et al., *Geant4—a simulation toolkit*, *Nucl. Inst. and Meth. in Phys. Res. Sect. A* **506** (2003) 250.
- [31] NEXT Collaboration, “NEXUS.” <https://github.com/next-exp/nexus>.

- [32] B. Al Atoum, S. Biagi, D. González-Díaz, B. Jones and A. McDonald, *Electron transport in gaseous detectors with a Python-based Monte Carlo simulation code*, *Computer Physics Communications* **254** (2020) 107357 [[1910.06983](https://arxiv.org/abs/1910.06983)].
- [33] NEXT collaboration, *Background rejection in NEXT using deep neural networks*, *Journal of Instrumentation* **12** (2017) T01004.
- [34] NEXT collaboration, *Demonstration of background rejection using deep convolutional neural networks in the NEXT experiment*, *Journal of High Energy Physics* **2021** (2021) 189.
- [35] NEXT collaboration, *Boosting background suppression in the NEXT experiment through Richardson–Lucy deconvolution*, *Journal of High Energy Physics* **2021** (2021) 146.
- [36] OSG, *Open Science Data Federation*, 2015. [10.21231/0KVZ-VE57](https://doi.org/10.21231/0KVZ-VE57).
- [37] OSG, *OSPool*, 2006. [10.21231/906P-4D78](https://doi.org/10.21231/906P-4D78).
- [38] R. Pordes, D. Petravick, B. Kramer, D. Olson, M. Livny, A. Roy et al., *The open science grid*, in *J. Phys. Conf. Ser.*, vol. 78 of 78, p. 012057, 2007, [DOI](https://doi.org/10.1088/1742-6596/78/1/012057).
- [39] I. Sfiligoi, D.C. Bradley, B. Holzman, P. Mhashilkar, S. Padhi and F. Wurthwein, *The pilot way to grid resources using glideinWMS*, in *2009 WRI World Congress on Computer Science and Information Engineering*, vol. 2 of 2, pp. 428–432, 2009, [DOI](https://doi.org/10.1109/WCSE.2009.5139070).

## A Natural Xenon Detector

The acceptance factors for a natural detector are shown in Fig. 12. Overall, the acceptance factors slightly improve on the enriched detector due to the higher signal containment.

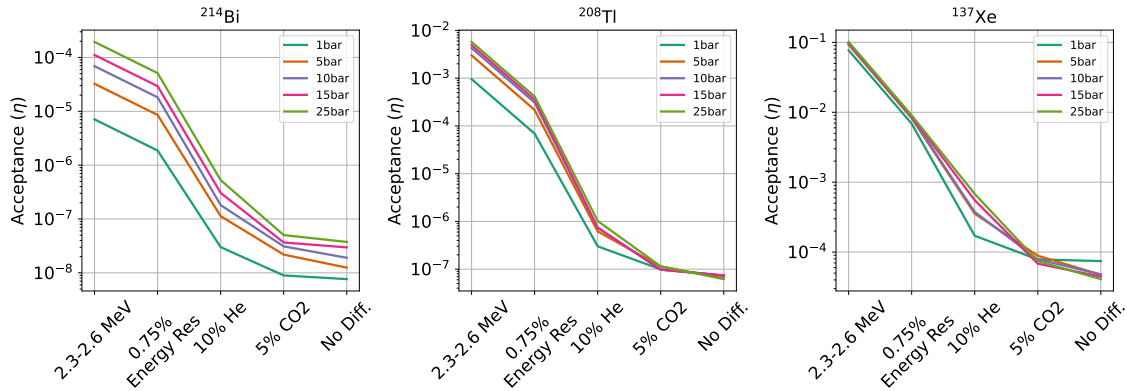


**Figure 12.** The total acceptance factors for each background category as a function of the analysis stage for a natural detector.

The total background rate for the natural detector is shown in Fig. 13. While there is a similar background rate for  $^{137}\text{Xe}$ , the  $^{214}\text{Bi}$  and  $^{208}\text{Tl}$  backgrounds do not perform as well due to the large mass copper shielding required.

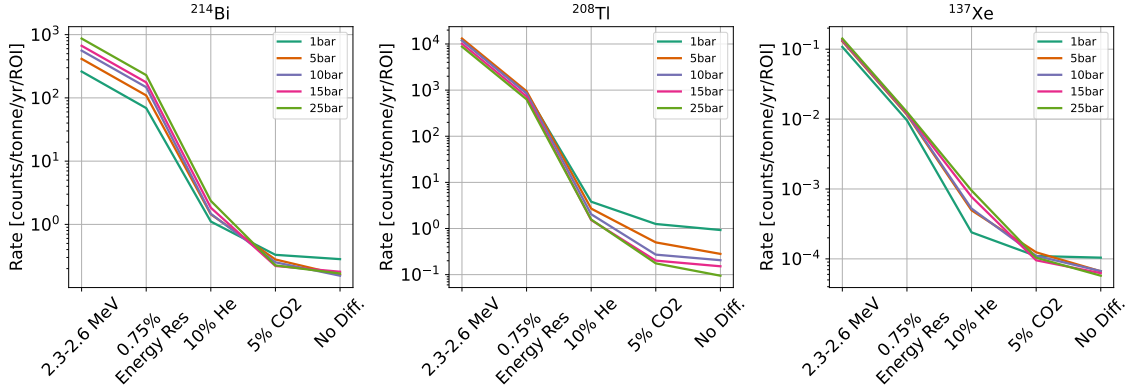


**Figure 13.** The total background rate for each background category as a function of the analysis stage for a natural detector.

## B Impact of Event Placement

The fiducial volume cut is powerful in reducing the surface background, such as Bi-Po from the copper surface and cathode. For technologies such as the Topology and Ion TPCs, S1 light may be quenched through the addition of molecular additives, requiring alternative ways to be developed to place events in the drift direction suitably. We explore the effectiveness of using topology selections without event position placement for (i) surface backgrounds and (ii) radon-induced backgrounds.

**Surface Background:** Figure 14 shows the rate with and without the application of the fiducial volume cut of 2 cm applied to the wall edges in a Topology TPC (assuming 5% CO<sub>2</sub> gas additive). For the enriched detector, the rate increase for 5% CO<sub>2</sub> is slightly larger at lower pressure with a maximal rate increase of  $\sim 0.1$  counts/tonne/yr/ROI. The natural detector also follows a similar trend with an increase in rate at lower pressure compared with higher.

**Radon:** To study the impact of <sup>214</sup>Bi at the cathode induced from <sup>222</sup>Rn, we follow the same simulation procedure as described in Sec. 3. <sup>214</sup>Bi events are generated (including subsequent decays and deexcitations to <sup>210</sup>Pb) at the surface of the detector face with the longest drift distance to model the placement of a cathode. <sup>214</sup>Bi decays were simulated resulting in  $\sim 200$ k events depositing energy within 1% FWHM of the  $Q_{\beta\beta}$ -value for each pressure. The containment rates and energy resolution cuts for this background are shown in Fig. 15. The containment fractions are increasing with pressure, while the reduction in background from energy resolution is similar in magnitude to <sup>208</sup>Tl/<sup>137</sup>Xe.

The selection performance with and without using a fiducial volume cut is shown in Fig. 16. Without any reconstruction inefficiencies, the radon background is reduced to a negligible level with a 2 cm fiducial volume cut. Removing the fiducial volume cut, background rejection factors are around 97-99.5% depending on pressure.

Radon activity reported by the NEXT-White experiment is 38.1 mBq/m<sup>3</sup> [27]. This background rate depends on the detector volume. The total acceptance factors using event topology without the fiducial volume cut range from  $2\text{-}7 \times 10^{-6}$  and would be insufficient

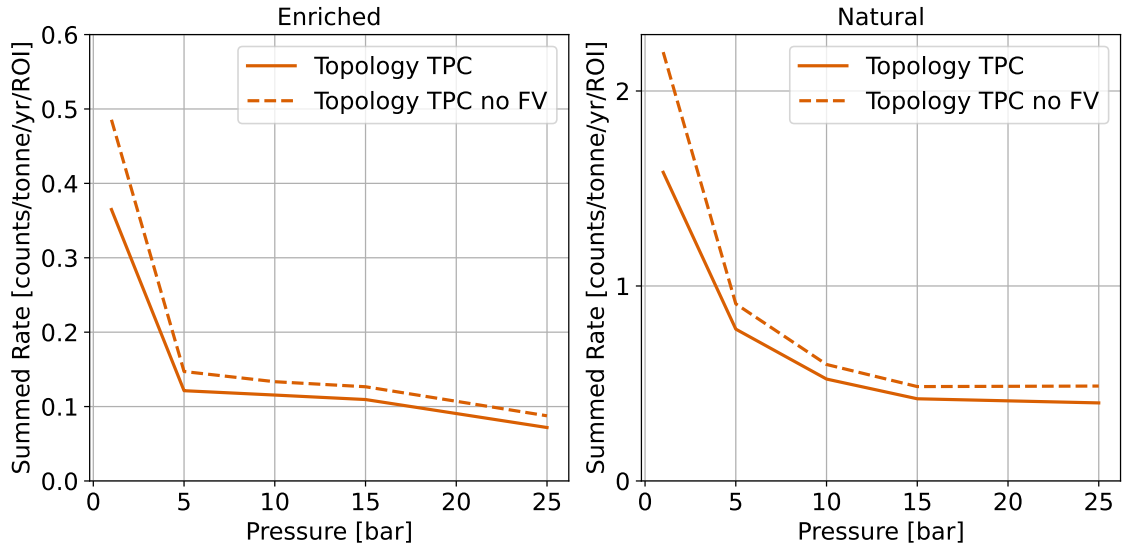


**Figure 14.** A summary of the summed background rate with and without the fiducial volume (FV) cut including  $^{214}\text{Bi}$ ,  $^{208}\text{Tl}$ , and  $^{136}\text{Xe}$ , for a Topology TPC assuming 5%  $\text{CO}_2$  gas additive. The left figure shows the performance for an enriched detector configuration, while the right figure shows a natural detector configuration. These performances assume a 0.75% FWHM energy resolution.

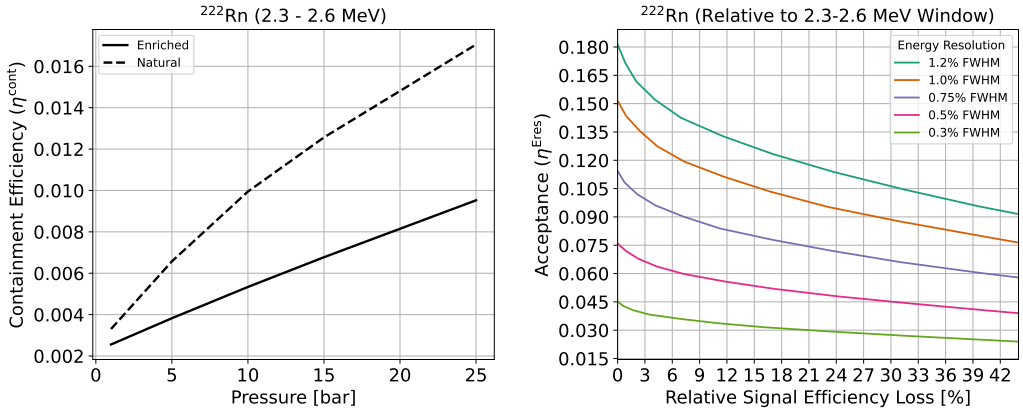


**Figure 15.** (left) The containment rates for  $^{214}\text{Bi}$  at the cathode induced from  $^{222}\text{Rn}$  as a function of pressure for an enriched and natural detector. (right) The background acceptance rates assuming different energy resolutions for  $^{214}\text{Bi}$  at the cathode induced from  $^{222}\text{Rn}$ . The x-axis shows the efficiency loss vs background acceptance from increasing the lower bound cut on energy.

for rejecting this background without additional means.

Of the selected radon events, a majority are from the 3.2 MeV beta electron stretching into the gas region. This is combined with a large energy deposition at the track start due to partial energy deposition from the 7.8 MeV alpha from the decay of  $^{214}\text{Po}$  which reduces the effectiveness of the blob energy cut. Analyses may utilize more advanced topological features, such as the straightness of the beta track near the track start or the larger diffusion to tag these cathode-originating events and improve performance. Furthermore, alternative

methods for suitable event placement could be employed with this technology, such as the identification of positive ion signals reaching the cathode.

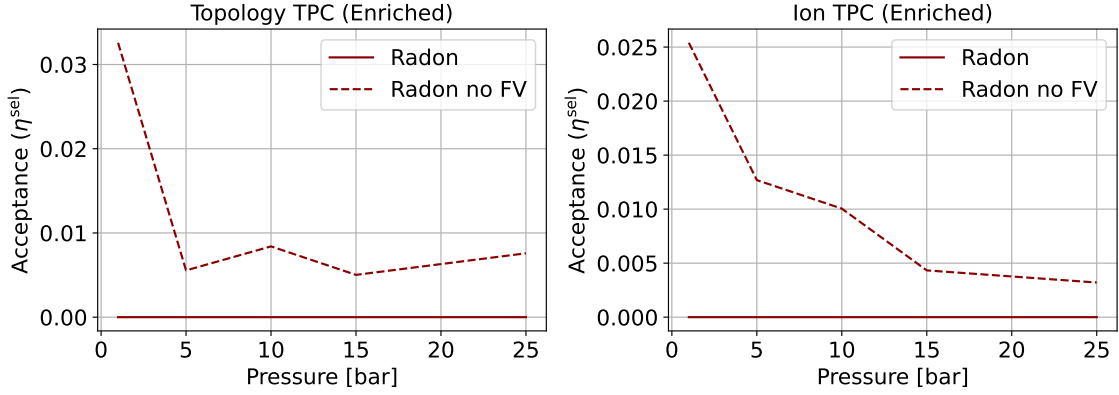


**Figure 16.** The selection rejection factors with and without a fiducial volume cut for (left) a Topology TPC and (right) an Ion TPC. A fiducial volume cut is able to reduce the radon background to negligible levels while some background remains without the fiducial volume cut.